coatings

MDPI

Article

Systematic First-Principles Investigations of the Nucleation, Growth, and Surface Properties of $Al_{11}RE_3$ Second-Phase Particles in Al-Based Alloys

Wei Yin [1,2], Yuming Liu [3], Lan Lin [1], Yiru Wang [2], Leyi Chen [2], Zhaoting Li [2], Honghu Peng [2], Touwen Fan [1,2,*], Yuanzhi Wu [1], Yuanxiang Deng [2], Xiong Liu [2] and Dongchu Chen [3,*]

[1] Research Institute of Automobile Parts Technology, Hunan Institute of Technology, Hengyang 421002, China; 17373958169@163.com (W.Y.); linlain123@163.com (L.L.); 2013001767@hnit.edu.cn (Y.W.)
[2] School of Science, Hunan Institute of Technology, Hengyang 421002, China; 13875094936@163.com (Y.W.); qishi5670@gmail.com (L.C.); dyx@hnit.edu.cn (Z.L.); 13575003362@163.com (H.P.); yxdeng@hnu.edu.cn (Y.D.); liuxiong_2022@163.com (X.L.)
[3] School of Material Science and Hydrogen Energy Engineering, Foshan University, Foshan 528001, China; jisuanzhanghao@163.com
* Correspondence: fantouwen@hotmail.com (T.F.); chendc@fosu.edu.cn (D.C.); Tel.: +86-0734-3452140 (T.F.); Fax: +86-0734-3452141 (T.F.)

Abstract: At room temperature, Al alloys have excellent mechanical properties and are widely used in automotive, electronics, aerospace and other fields, but it is difficult to maintain this advantage in the middle and high temperature ranges. To address this issue, second-phase $Al_{11}RE_3$ (RE represents rare earth element) was introduced into a Al-Mg-RE alloy as its primary constituent. By incorporating RE elements as additives, this material exhibits exceptional mechanical and thermal properties at elevated temperatures. Based on first principles and quasi-harmonic approximation (QHA), the nucleation growth mechanism and surface properties of second-phase $Al_{11}RE_3$ were studied in this paper. The interfacial energy $\gamma_{\alpha/\beta}$, strain energy ΔE_{CS} and chemical driving force ΔG_V of $Al_{11}RE_3$ were obtained. Models1, 4, and 6 have better properties of para-site connections than inter-site connections. It is found that the resistances of particle nucleation, interface energy $\gamma_{\alpha/\beta}$ and strain energy ΔE_{CS}, first increase and then decrease with increased atomic number REs, but they are much smaller than the chemical driving force ΔG_V. A reduced chemical driving force and a diminished nucleation radius R^* are more favorable for the process of nucleation. The addition of Sc is the most unfavorable for nucleation, and La has the strongest nucleating ability, which gradually decreases as the atomic number of the lanthanide element increases. The nucleation ability of the $Al_{11}RE_3$ phase decreases with increasing temperature, which is consistent with the experiments. The nucleation radius R^* also increases with increasing temperature, indicating that the nucleation ability decreases as the atomic number of the lanthanide elements increases. Since the smaller the nucleation radius R^* the easier the nucleation, compared with model4 and 6, model1 has a smaller nucleation radius R^* and the smallest increment. Thus, model1 is more prominent in the nucleation mechanism. In the particle growth study, the smaller the diffusion activation energy Q, the faster the diffusion rate in the Al matrix, and hence the higher the coiling rate, which promotes the growth of second-phase particles. The diffusion activation energy Q decreases sequentially from La to Ce and then increases with atomic number. The coarsening rate K_{LSW} of the $Al_{11}RE_3$ phase in models1, 4, and 6 increased with increasing temperature, which promoted the growth of particles. This paper is intended to provide a solid theoretical basis for the production and application of aluminum alloy at high temperatures.

Keywords: first-principles calculations; aluminum alloys; second phase; surface properties; nucleation and growth of particles

check for updates

Citation: Yin, W.; Liu, Y.; Lin, L.; Wang, Y.; Chen, L.; Li, Z.; Peng, H.; Fan, T.; Wu, Y.; Deng, Y.; et al. Systematic First-Principles Investigations of the Nucleation, Growth, and Surface Properties of $Al_{11}RE_3$ Second-Phase Particles in Al-Based Alloys. *Coatings* **2024**, *14*, 983. https://doi.org/10.3390/coatings14080983

Academic Editor: Raul Arrabal

Received: 29 June 2024
Revised: 30 July 2024
Accepted: 31 July 2024
Published: 4 August 2024

Copyright: © 2024 by the authors. Licensee MDPI, Basel, Switzerland. This article is an open access article distributed under the terms and conditions of the Creative Commons Attribution (CC BY) license (https://creativecommons.org/licenses/by/4.0/).

1. Introduction

Aluminum alloys have low density, strong weldability and high specific strength, which makes them widely used in the automotive, electronics and aerospace industries [1–5]. The addition of rare earth elements (RE) has become a feasible method to improve the performance of Al alloys, and much research has been done on this basis [6–8]. In detail, the addition of Sc atoms to the Al solution maximizes the percentage of solute strength per atom [9]. The addition of Sc to Al-Zr binary aluminum alloys leads to higher aluminum diffusivity and produces more and smaller precipitates for heterogeneous nucleation potential, providing a new starting point for mechanical behavior [10,11]. Similarly, adding Er to aluminum for an Al-Er system yields the characteristics of high hardness, high strength, grain refinement, and strong plasticity [12]. At the same time, the microalloying effect of RE can inhibit impurity damage [13]. Obviously, RE elements as additives can make materials with superior mechanical and thermal properties, which is an effective method to improve the comprehensive properties of target alloys [14–25].

Because of their excellent mechanical properties and service performance at room temperature, commercial aluminum alloys usually fit well with the goal of "light weight-high strength" [26], but this advantage is difficult to maintain in the medium-to-high temperature range. Today, in addition to classical commercial alloys such as W319 [27] and 2219 [28], there are currently Sc/Zr/Er-composite micro-alloyed Al-Sc-based alloys and Mg/Ag-composite micro-alloyed Al-Cu-based alloys [29]. These heat-resistant Al alloys for large structural components are very limited. The decay ratio of mechanical energy of the material in high-temperature service, relative to room temperature, is contingent upon both the high temperature stability inherent to the material itself and the corresponding ambient temperature. In order to enhance high-temperature performance in an aluminum alloy, we utilize Al-Mg-RE alloys with $Al_{11}RE_3$ as the primary second phase (where RE represents rare earth elements) and incorporate rare earth elements as additives to impart exceptional mechanical and thermal properties to the material. By conducting observations on the material's stability under high temperatures, it is possible to mitigate the detrimental impact of elevated temperatures on material strength, thereby addressing the issue of insufficient strength exhibited by materials in high-temperature environments [26].

The thermal stabilization of materials can be obtained by the selection of strengthening phase and the high-temperature stabilization of the second-phase particles. Heat-stabilized strengthening phases include ceramic phases represented by metal matrix composites (MMCs) and eutectic structures represented by classic Al-Fe-V-Si alloys, as well as precipitated phases and alloying strategies. The high-temperature stabilization of second-phase particles is studied via inhibition of Ostwald coarsening and coarsening kinetics in multiple systems [26].

With increasingly mature rapid solidification technology, the particle spacing between rod (needle)-shaped Al_3Ni [30–32] and laminar $Al_{11}Ce_3$ [33–36] has been successfully reduced to tens of nanometers, which can provide a considerable strengthening effect. Small amounts of transition metal elements (TM), such as Sc, Zr, V, etc., were added to form $L1_2$-type Al_3TM particles, which was another effective strengthening strategy. Among them, the insufficient solid solubility of TM can reduce the formation of crystalline phases and reduce the harm of plastic toughness to a certain extent. Pandey [31], Suwanpreecha [30] and Sims [34] et al. realized an $Al_3Ni/Al_{11}Ce_3$ + Al_3Sc/Al_3Zr dual-scale particle-reinforced alloy material in an aluminum base alloy, and determined its excellent high temperature mechanical properties in the temperature range of 250–300 °C [35]. The team of Professor Seidman and Professor Dunand proposed a series of Al-Sc-based heat-resistant aluminum alloy materials [1,37] and gradually refined a series of microalloying processes for elements such as Zr, Er, Si and their material design methods, and developed a series of well-known Al-Sc-Zr-Er-Si-based alloys [38–46]. The scientific research team of Academician Zuoren Nie took the lead in developing a series of aluminum alloys with Er instead of Sc microalloying [47].

It is well known that $Al_{11}RE_3$ particles play an important role as a major second phase in Al-Mg-RE alloys [48]. Specifically, these high melting points can effectively block

dislocation movement and grain boundary sliding during high temperature deformation, resulting in good resistance to high-temperature creep [25,41,49–51]. The exploration of interface properties between the matrix and the second phase is an important investigative direction [52–54]. Clearly, the stability and orientation relationships of the interface describe the nucleation driving force of second-phase particles and the parallel crystal plane or direction between the two phases on both sides of the interface, which is useful for the $Al_{11}RE_3$ nucleation mechanism [55,56]. Meanwhile, the diffusion behavior of dissolved impurity atoms directly affects the growth of $Al_{11}RE_3$ spherical particles [57,58], whereas the stable low-index surface properties of second-phase particles determines the toughness strength of binding bonds of particles to the matrix [59].

However, it is very difficult to study the nucleation and growth behavior of $Al_{11}RE_3$ particles due to the multi-variable nature and complexity of experiments [60–62]. Fortunately, in recent years, with the development of modern computer technologies, theoretical identification, e.g., first-principles (FP) calculations based on density functional theory (DFT), in complicated systems has become a powerful method in the field of metals and ceramics [63–71]. Herein, the nucleation mechanism and surface properties of $Al_{11}RE_3$ were investigated based on FP calculations using density functional theory (DFT). The relationship between the driving force and resistance of particle nucleation and the RE atomic number was found by calculation. In addition, the stability of the aluminum alloy relative to atomic number of RE was obtained from the surface energy calculated from the slab models of the material. The aim of this study is to improve second-phase high temperature stability in Al alloys and provide theoretical support for the development of heat-resistant Al alloys.

2. Computational Methodology

In this paper, first principles (FP) combined with density functional theory (DFT) were used to calculate Al alloys using Vienna ab initio simulation software package (VASP.5.4.4). The Kohn–Sham equation was solved by the total energy of plane wave method, and the valence electron density and wave function were obtained [72]. Electron–ion interactions were described using the projector augmented wave (PAW) [73,74] method, and the Perdew–Burke–Ernzerh (PBE) version of the generalized gradient approximation (GGA) [75] was used to treat the exchange-correlation functional. All structures were fully relaxed for volume as well as for all intracellular atomic coordinates. Considering the convergence of energy truncation and K-point results, we selected a plane wave base with truncation energy of 350 eV. The Monckhorst package method centered on gmma was adopted to set the grid of atomic cells as $8 \times 3 \times 3$ [76]. During calculation, the PAW_GGA pseudopotentials of Sc, Al-La, Al-Y_sv, Al-Ce_3, Al-Pr_3, and (Nd-Lu) were used to simulate the size of the real potential. For accurate calculations, the ground state geometric relaxation was minimized via conjugate gradients (CG) until the Hellmann–Feynman force was less than 0.01 eV/Å and the static total energy was calculated using the Methfessel–Paxton order N method until the total energy converged to 10^{-6} eV/atom.

The interface models of Al and AlRE were established through Materials Studio 8.0 software [77]. Low-index surfaces (0 0 1) and (0 1 0) of Al and $Al_{11}RE_3$ had 25 and 19 layers, respectively, while the Al/$Al_{11}RE_3$ interface (001-001) adopted 24, 26, and 24 layers. Interface (110-001) adopted 26, 26, and 24 layers, and interface (111-010) adopted 14 layers. Figure 1a shows the slab models for $Al_{11}RE_3$ (0 0 1) and (0 1 0), and a vacuum layer with a thickness of 15 Å was added at both ends of the models to avoid interaction between the two ends of the model. Note: the right image in Figure 1a shows the corresponding $Al_{11}RE_3$ (0 0 1) and (0 1 0) surfaces, named as AlRE1 and AlRE2 terminals. Due to the difference between the AlRE1 and AlRE2 terminals, the $Al_{11}RE_3$ (001) | | Al (001) and the $Al_{11}RE_3$ (001) | | Al (010) interface models are drawn in Figure 1b, and Model1–3 belong to $Al_{11}RE_3$ (001) | | Al (001), but the model is different due to different atom positions; model4–6 are the same as above. At the same time, the six models can be divided into interpositions (model2, 3, and 5) and propositions (model1, 4, and 6) according to the different atomic positions. After rigorous

convergence tests, 8 × 3 × 1 grids were used for all interface models to ensure the accuracy of the data, and 4 × 10 × 1 and 9 × 3 × 1 grids were applied for slab1 and slab2 models, respectively. It is hoped that the calculation study in this paper can be applied to Al alloys urgently needed for the medium temperature interval in the current industry, and provide a reference for research on high-temperature thermal stability of Al alloys.

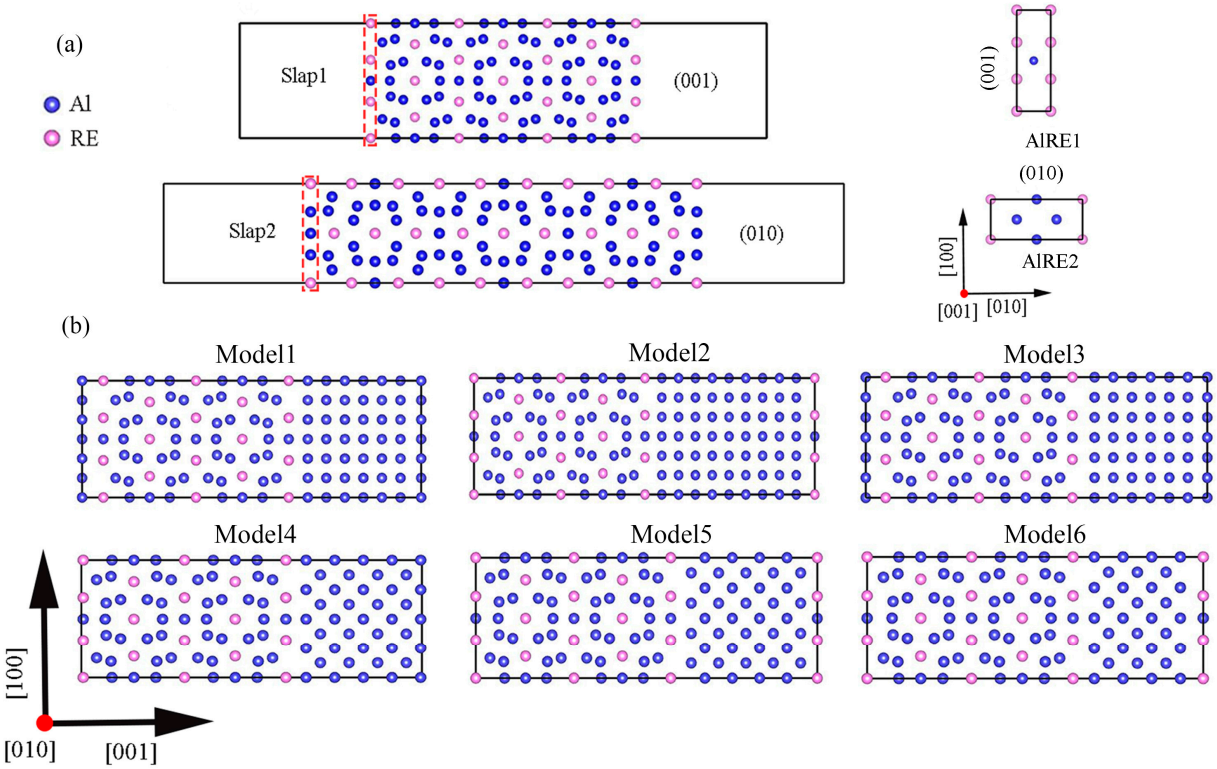


Figure 1. (**a**) The slab model; (**b**) $Al_{11}RE_3$ (001) | | Al (001) interface model of model1–3, and $Al_{11}RE_3$ (001) | | Al (010) interface model of model4–6.

3. Result and Discussion

3.1. Surface Activity

According to the Hutchinson–Rice–Rosengren (HRR) theory [78,79], the surface energy can be used to characterize the effect of different $Al_{11}RE_3$ compositions on the hardness of aluminum alloys, and the greater the surface energy, the greater the hardness of the material.

For Al (0 0 1) surface, its surface energy is calculated as in formula [80]

$$E_{sur} = \frac{E_{Al}^{slab} - N \times \mu_{Al}^{bulk}}{2A} \quad (1)$$

where E_{Al}^{slab}, N, and μ_{Al}^{bulk} are the total energy of the aluminum plate model, number of Al atoms in the slab mode and chemical potential of one atom in the bulk aluminum, respectively

For $Al_{11}RE_3$, the surface energy calculation for both interfaces can be expressed by the following formula [59]:

$$E_{sur} = \frac{E_{slab} - N_{Al} \times \mu_{Al}^{slab} - N_{RE} \times \mu_{RE}^{slab}}{2A} \quad (2)$$

where E_{sur}, E_{slab}, N_i and A are the surface energy of each model, total energy of the completely relaxed plate, and atomic number of RE or Al in the surface model and area of the terminating surface, respectively; μ_i^{slab} and μ_i^{bulk} are the chemical potential of Al or RE atoms in the slab plate and the chemical potential of the bulk i.

Similarly,

$$11\mu_{\mathrm{Al}}^{\mathrm{slab}} + 3\mu_{\mathrm{RE}}^{\mathrm{slab}} = \mu_{\mathrm{Al_{11}RE_3}}^{\mathrm{bulk}} \tag{3}$$

$$E_{\mathrm{sur}} = \frac{E_{\mathrm{slab}} - N_{\mathrm{RE}} \times \mu_{\mathrm{Al_{11}RE_3}}^{\mathrm{bulk}} - (11N_{\mathrm{RE}} - 3N_{\mathrm{Al}}) \times \mu_{\mathrm{Al}}^{\mathrm{slab}}}{2A} \tag{4}$$

Thus, the surface energy E_{sur} of a stoichiometric ($11N_{\mathrm{RE}} = 3N_{\mathrm{Al}}$) surface can be defined as:

$$E_{\mathrm{sur}} = \frac{E_{\mathrm{slab}} - 3N_{\mathrm{RE}} \times \mu_{\mathrm{Al_{11}RE_3}}^{\mathrm{bulk}}}{2A} \tag{5}$$

The thermodynamic stability of a material is usually expressed by the enthalpy of formation (ΔH^{f}),

$$11\mu_{\mathrm{Al}}^{\mathrm{bulk}} + 3\mu_{\mathrm{RE}}^{\mathrm{bulk}} + \Delta H^{\mathrm{f}} = \mu_{\mathrm{Al_{11}RE_3}}^{\mathrm{bulk}} \tag{6}$$

Combining Formulas (3) and (6), we obtain:

$$11\mu_{\mathrm{Al}}^{\mathrm{bulk}} + 3\mu_{\mathrm{RE}}^{\mathrm{bulk}} + \Delta H^{\mathrm{f}} = 11\mu_{\mathrm{Al}}^{\mathrm{slab}} + 3\mu_{\mathrm{RE}}^{\mathrm{slab}} \tag{7}$$

$$3\mu_{\mathrm{RE}}^{\mathrm{bulk}} - 3\mu_{\mathrm{RE}}^{\mathrm{slab}} + \Delta H^{\mathrm{f}} = 11\left(\mu_{\mathrm{Al}}^{\mathrm{slab}} - \mu_{\mathrm{Al}}^{\mathrm{bulk}}\right) \tag{8}$$

The formation enthalpy of $Al_{11}RE_3$ can be derived from the same article. The formation enthalpy (ΔH^{f}) is all negative, indicating that there is a strong interaction between atoms and the material has good stability. From this, the chemical potential range of Al can be obtained:

$$\frac{1}{11}\Delta H^{\mathrm{f}} < \mu_{\mathrm{Al}}^{\mathrm{slab}} - \mu_{\mathrm{Al}}^{\mathrm{bulk}} < 0 \tag{9}$$

For non-stoichiometric surfaces, the surface energy can be expressed according to [59,81–83]:

$$E_{\mathrm{sur}} = \frac{E_{\mathrm{slab}} - N_{\mathrm{RE}} \times \mu_{\mathrm{Al_{11}RE_3}}^{\mathrm{slab}} - (11N_{\mathrm{RE}} - 3N_{\mathrm{Al}}) \times \left(\mu_{\mathrm{Al}}^{\mathrm{bulk}} + \left(\mu_{\mathrm{Al}}^{\mathrm{slab}} - \mu_{\mathrm{Al}}^{\mathrm{bulk}}\right)\right)}{2A} \tag{10}$$

The surface energy E_{sur} results are derived from Formulas (2)–(10); the range values are shown in Figure 2. It can be seen that the two curves of slab1 and slab2 have the same trend: the slab1 curve reaches the highest value at Sc, showing a wavy trend, starting from Pr and showing a steady upward and downward fluctuation trend; the slab2 curve is at Sc at the lowest point, rising rapidly from Sc to Y, then decreases at La, and then arches.

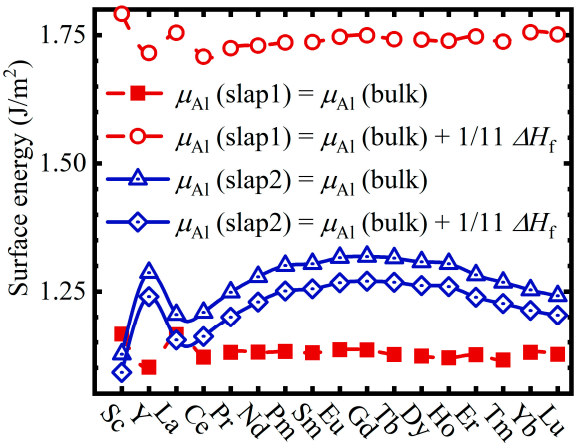


Figure 2. The calculated non-metered surface energy range values.

The curve rises slowly and starts to decline at Gd. Combined with the different environmental conditions of the $Al_{11}RE_3$ surface, the results indicate that the surface energies of the non-stoichiometric termination of the $Al_{11}RE_3$ (001) and (010) planes both

vary with the chemical potential of Al. In an Al-rich atmosphere, $\mu_{Al}^{slab} = \mu_{Al}^{bulk}$; in an Al-poor atmosphere, $\mu_{Al}^{slab} = \mu_{Al}^{bulk} + \frac{1}{11}\Delta H^{f}$. The results show that in the slab1 model, the E_{sur} of $Al_{11}RE_3$-AlRE1 terminal ranges from 1.10 to 1.16 J/m^2 in an Al-rich atmosphere, and the E_{sur} in an Al-poor atmosphere ranges from 1.71 to 1.79 J/m^2. The E_{sur} of the $Al_{11}RE_3$-AlRE2 terminal in an Al-rich atmosphere ranges from 1.13 to 1.32 J/m^2 whereas the E_{sur} in an Al-poor atmosphere ranges from 1.10 to 1.27 J/m^2.

3.2. Driving and Hindering Forces

Based on classical nucleation theory (CNT) [61,84], the thermodynamic barrier for nucleation is controlled by competition; this study discusses the nucleation characteristics of $Al_{11}RE_3$ particles in the Al matrix: (1) positive interfacial free contribution energy $\gamma_{\alpha/\beta}$; (2) positive strain energy ΔE_{CS}; (3) negative free energy contribution difference ΔG_V [85].

Based on the non-metric surface energy derived from the above, and $\mu_{Al}^{slab} = \mu_{Al}^{bulk}$, the non-metric interfacial energy formula of the aluminum alloy can be obtained as follows [80]:

$$\gamma_{\alpha/\beta} = [\frac{E_{total} - N_{RE} \times \mu_{Al_{11}RE_3}^{bulk} + (11N_{RE} - 3N_{Al,1}) \times \left(\mu_{Al}^{bulk} + \left(\mu_{Al}^{slabd} - \mu_{Al}^{bulk}\right)\right) - N_{Al,2} \times \mu_{Al}^{bulk}}{A}] - \gamma_{s,Al(001)} - \gamma_{s,Al_{11}RE_3} \quad (11)$$

where E_{total}, $\gamma_{s,i}$, $N_{Al,1}$ and $N_{Al,2}$ are the total energy of the relaxed interface model, surface energy of the Al (0 0 1) or $Al_{11}RE_3$ (0 0 1) surface, number of Al atoms in the AlRE layer, and number of Al layers, respectively.

Due to the twisting of the respective lattices, coherent strain energies are generated to obtain a common interface between the parent and precipitated phases. Taking into account the harmonic strain energy and anharmonic strain energy, the strain energy of the phase was calculated using density functional theory. It can be calculated by [84,86]:

$$\Delta E_{cs}(x, \hat{G}) = \min_{\alpha_s}(x\Delta E_{\alpha}^{eqi}(\alpha_s, \hat{G}) + (1+x)\Delta E_{\beta}^{eqi}(\alpha_s, \hat{G})) \quad (12)$$

where α_s is the constrained superlattice parameter, $\hat{G}$ is the direction, and x is the mole fraction of phase α and β; E_{α}^{eqi} and ΔE_{β}^{eqi} are the epitaxial deformation energies of phases α and β, respectively.

Table 1 shows the calculated values of the interfacial energy and strain energy of $Al_{11}RE_3$ in Al, along with other calculated values [87], and the data graphs are shown in Figure 3a,b. It can be seen that the calculated interface energy of 0.58 J·m^{-2} for the $Al_{11}Ce_3$(00l) | Al(001) system is comparable to the value of 0.698 J·m^{-2} calculated by Zhang et al. [87], indicating the correctness and reliability of our investigation. According to the observations in Figure 3a,b, the trend of interface energy and strain energy tends to be consistent. There is a strong relationship with the atomic number of the rare earths: the value is the lowest at Sc, increases towards La and reaches its peak there, and then shows a downward trend with increasing RE atomic number. For Al/$Al_{11}RE_3$ interfaces, $\gamma_{\alpha/\beta}$ is in the order of $\gamma_5 < \gamma_2 < \gamma_3 < \gamma_1 < \gamma_4 < \gamma_6$. Models4–6 are composed of the same Al and $Al_{11}RE_3$ surfaces. The interfaces of model4 and model6 are connected in alignment, and the interface energy is similar, while the interface energy value of model5 is the smallest, which may be due to the alignment of Al(010) and $Al_{11}RE_3$, and indicates that this interface is the easiest to form. Compared with the interface energy, the strain energy is sorted from smallest to largest as $\Delta E_{cs3} < \Delta E_{cs2} < \Delta E_{cs1} < \Delta E_{cs6} < \Delta E_{cs5} < \Delta E_{cs4}$.

The chemical formation energy variation ΔG_V of $Al_{11}RE_3$ precipitates can be expressed in dilute solid solution-based thermodynamics via $Al_nRE_3 \rightarrow Al_{11}RE_3 + Al_{n-11}$; the calculation is as follows [84]:

$$\Delta G_V = \Delta G_{Al_{11}RE_3} + (n - 11)\Delta G_{Al} - \Delta G_{Al_nRE_3} \quad (13)$$

where n is the atomic number and ΔG_i is the Gibbs free energy of $Al_{11}RE_3$ bulk, Al in the most stable bulk and solid solution Al_nRE_3, respectively. To study the dependence of ΔG_V on temperature, the non-equilibrium free energy ΔG_V can be expressed as [88,89]:

$$G(V, P, T) = \min[F(V, T)] + PV \quad (14)$$

where $F(V, T)$ is the free energy computed by the sum of electronic internal energy and phonon Helmholtz free energy $F(V, T) = U_{el} + F_{vib}$. P is the circumstantial pressure.

The calculated values of the driving force ΔG_V are shown in Table 2, and the chemical driving force ΔG_V of the second particles as a function of atomic number and temperature (~1000 K) is depicted in Figure 3c,d. In Figure 3c, it is clearly seen that at the temperatures of 100 K, 300 K, 600 K, and 900 K, the variation in the chemical driving force of the intermetallic particle with changes in atomic number reaches the peak at Sc, then decreases to the lowest point (La), and then increases as the atomic number increases. From Figure 3d, the ΔG_V of the particles increases slowly with increases in temperature, except for the ΔG_V of $Al_{11}Sc_3$.

Table 1. Calculated interfacial and strain energy values for model1–model6 in $Al_{11}RE_3$.

System	Model1		Model2		Model3		Model4		Model5		Model6	
	$\gamma_{\alpha/\beta}$	ΔE_{CS}	$\gamma_{\alpha/\beta}$	ΔE_{CS}	$\gamma_{\alpha/\beta}$	ΔE_{CS}	$\gamma_{\alpha/\beta}$	ΔE_{CS}	$\gamma_{\alpha/\beta}$	ΔE_{CS}	$\gamma_{\alpha/\beta}$	ΔE_{CS}
$Al_{11}Sc_3$	0.14	5.84	−0.62	5.21	−0.52	5.00	0.35	12.18	−0.21	6.77	0.32	11.13
$Al_{11}Y_3$	0.42	13.56	0.05	11.97	0.11	9.62	0.79	23.08	−0.03	21.30	0.83	16.95
$Al_{11}La_3$	0.56	26.09	0.43	22.30	0.52	20.79	0.98	37.28	0.21	34.12	1.04	27.30
$Al_{11}Ce_3$	0.58; 0.698 [87]	23.44	0.39	20.28	0.46	19.70	0.95	33.65	0.18	32.45	1.00	25.71
$Al_{11}Pr_3$	0.57	21.67	0.38	18.04	0.43	17.86	0.95	31.09	0.15	30.23	0.99	23.58
$Al_{11}Nd_3$	0.56	19.68	0.36	16.39	0.40	15.98	0.94	29.18	0.12	28.33	0.98	21.93
$Al_{11}Pm_3$	0.54	18.17	0.31	15.34	0.36	14.27	0.93	27.32	0.09	26.61	0.96	20.46
$Al_{11}Sm_3$	0.52	17.14	0.28	14.11	0.31	13.01	0.91	26.10	0.07	25.39	0.94	19.42
$Al_{11}Eu_3$	0.50	15.74	0.23	12.91	0.26	11.67	0.89	24.72	0.05	23.96	0.93	18.28
$Al_{11}Gd_3$	0.48	14.53	0.15	12.75	0.20	10.58	0.87	23.57	0.02	22.59	0.90	17.25
$Al_{11}Tb_3$	0.46	13.65	0.09	11.80	0.16	9.74	0.84	22.78	−0.01	21.57	0.87	16.70
$Al_{11}Dy_3$	0.44	12.91	0.04	11.26	0.11	9.01	0.80	22.17	−0.03	20.54	0.83	16.85
$Al_{11}Ho_3$	0.38	13.24	−0.01	10.60	0.08	8.28	0.77	21.70	−0.05	19.60	0.79	17.01
$Al_{11}Er_3$	0.36	12.79	−0.07	9.62	0.03	7.66	0.74	21.17	−0.08	18.70	0.76	16.63
$Al_{11}Tm_3$	0.34	11.93	−0.11	8.97	0.00	6.97	0.72	20.14	−0.11	17.69	0.73	16.01
$Al_{11}Yb_3$	0.32	11.36	−0.15	8.43	−0.01	6.53	0.70	19.12	−0.12	16.31	0.71	15.37
$Al_{11}Lu_3$	0.32	10.31	−0.16	7.59	−0.04	5.92	0.70	17.83	−0.12	14.73	0.70	14.54

Table 2. Calculated value of driving force ΔG_V at 0–1000 K.

Temperature / System	0 K	100 K	200 K	300 K	400 K	500 K	600 K	700 K	800 K	900 K	1000 K
$Al_{11}Sc_3$	−0.16	−1.21	−5.20	−10.45	−16.50	−23.30	−30.93	−39.54	−49.35	−60.65	−73.30
$Al_{11}Y_3$	−346.45	−344.08	−335.36	−324.80	−313.97	−303.38	−293.29	−283.93	−275.53	−268.39	−262.36
$Al_{11}La_3$	−702.96	−697.85	−679.25	−656.42	−632.40	−608.05	−583.72	−559.63	−535.97	−512.93	−490.22
$Al_{11}Ce_3$	−667.30	−662.57	−645.30	−624.09	−601.72	−578.99	−556.21	−533.58	−511.25	−489.40	−467.66
$Al_{11}Pr_3$	−610.96	−606.44	−589.96	−569.69	−548.32	−526.60	−504.85	−483.24	−461.94	−441.10	−420.37
$Al_{11}Nd_3$	−561.88	−557.56	−541.80	−522.49	−502.21	−481.71	−461.31	−441.20	−421.58	−402.66	−384.14
$Al_{11}Pm_3$	−514.29	−510.20	−495.30	−477.09	−458.04	−438.87	−419.92	−401.40	−383.52	−366.54	−350.19
$Al_{11}Sm_3$	−477.42	−473.59	−459.64	−442.59	−424.79	−406.92	−389.30	−372.16	−355.71	−340.21	−325.42
$Al_{11}Eu_3$	−437.48	−433.74	−420.08	−403.43	−386.11	−368.80	−351.83	−335.43	−319.85	−305.36	−291.77
$Al_{11}Gd_3$	−397.41	−393.80	−380.62	−364.55	−347.87	−331.24	−314.99	−299.37	−284.61	−271.02	−258.41
$Al_{11}Tb_3$	−363.03	−359.65	−347.24	−332.14	−316.51	−301.01	−285.96	−271.60	−258.20	−246.05	−235.01
$Al_{11}Dy_3$	−329.73	−326.52	−314.68	−300.26	−285.34	−270.57	−256.25	−242.64	−229.98	−218.59	−208.30
$Al_{11}Ho_3$	−298.29	−295.33	−284.30	−270.84	−256.94	−243.22	−229.99	−217.50	−206.01	−195.83	−186.82
$Al_{11}Er_3$	−267.61	−264.95	−254.81	−242.36	−229.45	−216.66	−204.28	−192.53	−181.65	−171.92	−163.16
$Al_{11}Tm_3$	−239.40	−236.98	−227.60	−216.04	−204.07	−192.27	−180.90	−170.19	−160.39	−151.78	−144.19
$Al_{11}Yb_3$	−207.63	−205.27	−196.03	−184.62	−172.81	−161.16	−149.96	−139.43	−129.81	−121.40	−114.02
$Al_{11}Lu_3$	−184.02	−182.39	−175.31	−166.42	−157.29	−148.42	−140.07	−132.47	−125.86	−120.55	−116.36

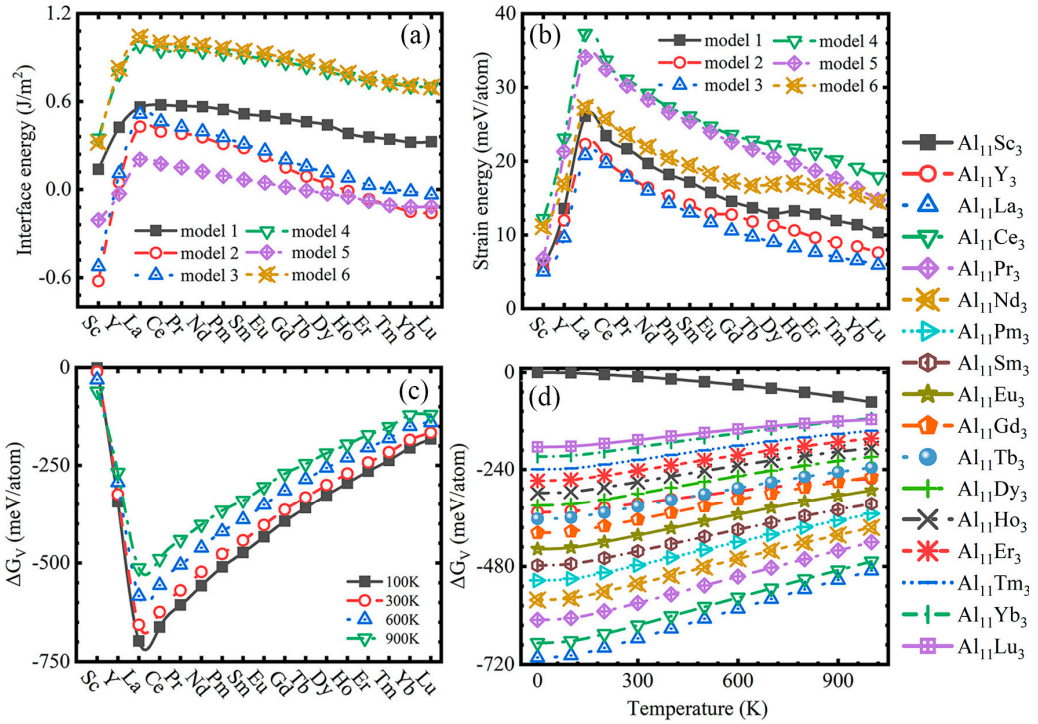


Figure 3. (**a**) The interface energy $\gamma_{\alpha/\beta}$, (**b**) strain energy ΔE_{CS} and (**c**) variation in chemical potential ΔG_V with atomic number at different temperatures; (**d**) variation in chemical potential ΔG_V among different Al alloy particles with temperature.

3.3. Particle Nucleation and Growth

For isolated uniform nucleation, the precipitates are spherical during growth, so it is a reasonable solution to use a spherical model for calculation. The total free energy for nucleation (ΔG_{tot}) can be expressed as [84]:

$$\Delta G_{tot} = \frac{4}{3}\pi R^3(\Delta G_V + \Delta E_{cs}) + 4\pi R^2\gamma \tag{15}$$

when

$$\frac{\partial G_{tot}}{\partial R} = 0 \tag{16}$$

The nucleation radius R^* can be expressed as:

$$R^* = -\frac{2\gamma}{\Delta G_V + \Delta E_{CS}} \tag{17}$$

The calculation results of the nucleation radius R^* are shown in Figure 4a–f, and Figure 4a–c are the curves of the nucleation radius R^* in model1, model4 and model6 as a function of the atomic number of lanthanide rare earths, respectively. Figure 4d–f shows the nucleation radius R^* versus temperature for model1, model4, and model6. It can be seen from Table 1 and Figure 3b that the interface energies $\gamma_{\alpha/\beta}$ of some elements in model2, model3, and model5 are negative values, so the nucleation radius R^* and the coarsening rate K_{LSW} cannot be calculated. Meanwhile, the Sc and Y elements in model1–model6 are unstable. Therefore, in order to understand the nucleation radius R^* characteristics of aluminum alloys more clearly and systematically, this paper only includes the lanthanide elements (La–Lu) from model1, model4 and model6 in the study.

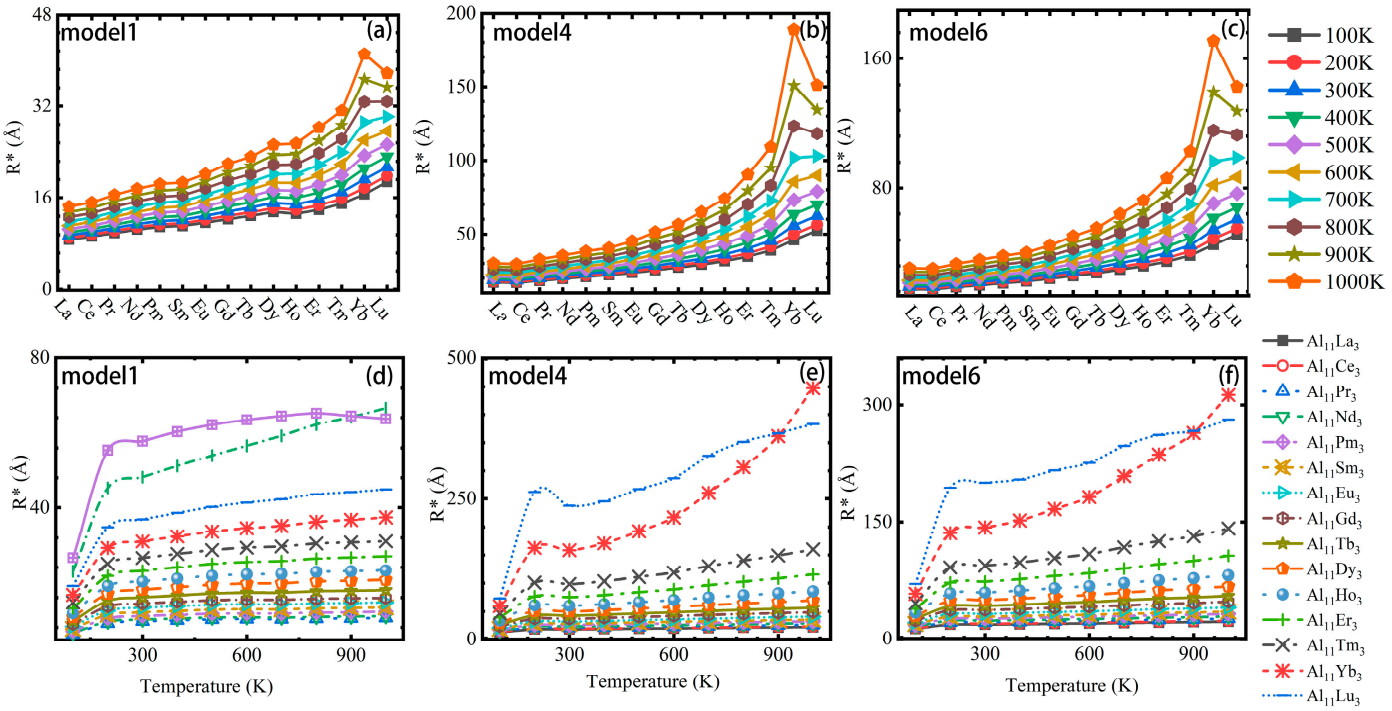


Figure 4. (**a**–**c**) The relationship between model1, model4 and model6's nucleation radius *R** as a function of atomic number; (**d**–**f**) the curve of nucleation radius *R** of model1, model4 and model6 as a function of temperature.

Combining Figure 4a–c, it can be observed that at 100–1000 K, the nucleation radius R^* of $Al_{11}RE_3$ generally increases with increasing atomic number of the lanthanide rare earths; but at high temperatures above 700 K, Lu decreases because the pseudopotential of Lu cannot well describe the interactions between atoms. The relationship between the nucleation radius *R** of model1, model4, and model6 and the lanthanide atomic number is consistent with the trend, but the values are quite different. Taking 1000 K as an example, in model1, the nucleation radius of lanthanide atoms rises from 14 Å to 41 Å as atoms enlarge from La to Yb. In model4, the La atom is 30 Å and the Yb atom rises to 189 Å. Model6 goes from 30 Å to 170 Å. It can be clearly seen from the model 4 that the largest and biggest increase nucleation radius *R**. But in fact, a smaller *R** is more conducive to nucleation, so the nucleation mechanism of model 1 is preferable. According to Figure 4d,e, the nucleation radius *R** generally shows an upward trend with the increase in temperature. At 100–200 K, the growth rate is the largest, and after 200 K, the growth rate shows a state of slow growth.

The nucleation radius *R** is used to detect the strength of the material's nucleation ability; to observe the growth of the particles, it is necessary to calculate the coarsening rate K_{LSW} of the material. The growth of $Al_{11}RE_3$ particles can be detected by coarsening according to the methods of Lifshitz and Slyozov [90] and Wagner [91] (LSW). The coarsening rate K_{LSW} is calculated as follows [57,58]:

$$K_{LSW} = \frac{8\gamma D\varepsilon_\infty V_m}{9RT} \quad (18)$$

where γ and R are the interface energy and the gas constant, respectively. D, ε_∞ and V_m are the diffusion coefficient of solute atoms, the solute concentration at equilibrium and solute molar volume, respectively.

To calculate the coarsening rate K_{LSW} of the particles, it is necessary to first calculate the diffusion coefficient D of the solute atoms and V_∞ in the equilibrium state, which are

determined by the chemical potential of the bulk and the energy barrier of the diffusion activation energy Q. Their values can be obtained by Formulas (19) and (20):

$$D(T) = a^2 v \exp(-\frac{Q}{kT}) \tag{19}$$

$$\varepsilon_\infty = \exp(\frac{\Delta G_V(Al_{11}RE_3)}{k_B T}) \tag{20}$$

where a and v are the transition distance and vibration frequency of each atom, respectively. The calculation results are shown in Figure 5a–g.

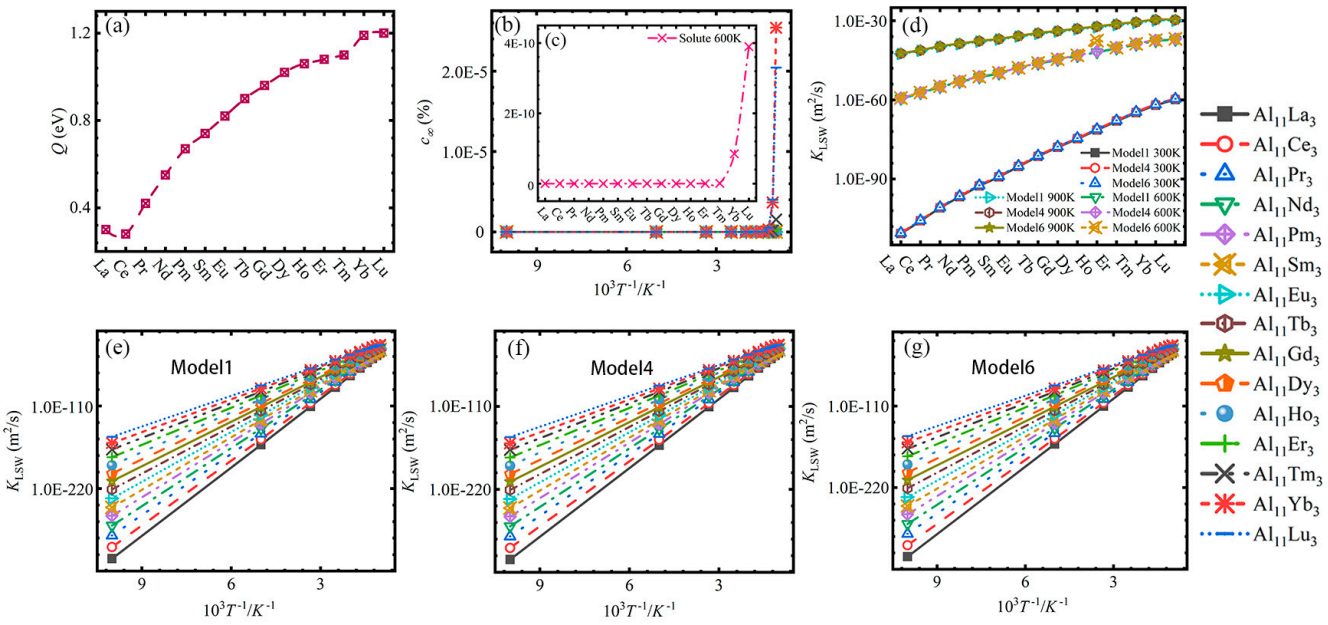


Figure 5. (**a**) The function of diffusion activation energy Q as a function of rare earth atomic number; (**b**,**c**) solute concentration ε_∞ as a function of temperature and the relationship between solute and rare earth atomic number at 600 K, respectively; (**d**) coarsening rate K_{LSW} as a function of rare earth atomic number for model1, model4 and model6; (**e**–**g**) coarsening rate K_{LSW} of model1, model4 and model6 as a function of temperature.

In the particle growth study, the smaller the diffusion activation energy Q, the faster the REE diffusion rate in the Al matrix, and hence the higher the coiling rate, which promotes the growth of second-phase particles. It can be seen from Figure 5a that the diffusion activation energy Q first decreases and then increases with the increase in the atomic number of lanthanide rare earths. Although there is a decrease from La to Ce, the decrease is smaller, being only from 0.3 eV of La to 0.28 eV, a decrease of about 6.7 percentage points; then, the diffusion activation energy Q increases with the increase in atomic number, reaching 1.2 eV. This indicates that the diffusion rate of rare earth elements in the Al matrix decreases with the increase in atomic number. Figure 5b shows that as the temperature increases, the solute concentration ε_∞ also increases. Observing Figure 5c, it can also be seen that at 600 K, the solid solubility ε_∞ increases with the increase in the atomic number of lanthanide rare earths: the growth rate is less obvious from La to Tm elements, but from Tm to Lu, the growth rate of the solid solubility ε_∞ greatly increased. From the diffusion activation energy Q and the solute concentration ε_∞ obtained above, the coarsening rate K_{LSW} is obtained by the formula as shown in Figure 5d–g. In Figure 5d, it is observed that at the same temperature, the coarsening rate K_{LSW} in model1, model4 and model6 are basically the same, and they all increase with the increase in rare earth atomic number, and the upward trend in each model also tends to be consistent. At the same time, the coarsening rate K_{LSW} of the model increases the most at 300 K and the

least at 900 K. Through Figure 5e–g, it can be observed that the coarsening rate K_{LSW} of $Al_{11}RE_3$ is proportional to the temperature, and both increase linearly with the increase in temperature. However, the growth rate shows a downward trend with the increase in the RE atomic number, which indicates that the coarsening rate K_{LSW} of $Al_{11}La_3$ is greatly affected by temperature, and the opposite for $Al_{11}Lu_3$.

4. Conclusions

AlRE1 and AlRE2 were established according to different surface models, and the interface models $Al_{11}RE_3$ (001) | | Al (001) and $Al_{11}RE_3$ (001) | | Al (010) were formed according to different pairings of para-positions and interpositions, and were named as model1–6 in turn. Based on the surface interface characteristics and nucleation growth characteristics of $Al_{11}RE_3$, the relationship between nucleation and atomic number of RE in alloys was studied through first-principles calculation. The following conclusions were obtained:

The results show that the nucleation growth in Al/AlRE interface model1–6 is related to the atomic number of the RE elements, especially lanthanides. In the nucleation mechanism, both the interfacial energy $\gamma_{\alpha/\beta}$ and strain energy ΔE_{CS} indicate nucleation resistance, which first increases and then decreases with the increase in atomic number. They first rise from the lowest point at Sc to La, and in the lanthanides, they decline as the atomic number rises.

At 100 K, 300 K, 600 K and 900 K, the chemical driving force ΔG_V of intermetallic compound particles first decreases and then increases with the increase in atomic number of RE. Taking the element La as the inflection point, it rises from La to Lu as the atomic number of the lanthanides increases. The interfacial energy $\gamma_{\alpha/\beta}$ and strain energy ΔE_{CS} are much smaller than the chemical driving force, and then the chemical driving force ΔG_V plays a major role in particle nucleation. The results show that the addition of Sc is the most unfavorable to nucleation, the nucleation ability of La is the strongest, and the nucleation ability gradually decreases with increases in lanthanide atomic number. In the relationship between chemical driving force and temperature, except for $Al_{11}Sc_3$, all other $Al_{11}RE_3$ phases all showed a slow upward trend with the increase in temperature, and the chemical driving force ΔG_V still increased with the increase in lanthanide atomic number. It shows that the nucleation ability of $Al_{11}RE_3$ phase decreases with the increase in temperature, which is consistent with objective fact.

Since the interface energy $\gamma_{\alpha/\beta}$ of some elements in models2, 3, and 5 is negative, the nucleation radius R^* and coarsening rate K_{LSW} cannot be calculated. At the same time, Sc and Y in models1 to 6 are unstable. In order to understand the nucleation and growth characteristics of aluminum alloys more clearly and accurately, only the lanthanides (La–Lu) in models1, 4 and 6 were included in the study. It has been shown that the nucleation radius R^* increases with the atomic number but decreases at Lu, which may be due to the fact that Lu's pseudopotential does not describe the interaction between atoms well. Meanwhile, the nucleation radius R^* also increases with increasing temperature, indicating that particle nucleation ability decreases with increasing atomic number of lanthanide elements. Since a smaller nucleation radius R^* leads to easier nucleation, model1 has a smaller nucleation radius R^* and the smallest increase compared to models4 and 6. Thus, model1 is more relevant to the nucleation mechanism.

In the study of particle growth, the smaller the diffusion activation energy Q, the faster the diffusion rate of the rare earth elements in the Al matrix, and thus the higher the coarsening rate, the more promoted the growth of second-phase particles. The diffusion activation energy Q decreases from La to Ce, and then increases with the increase in atomic number. The solid solubility ε_∞ of the particles increases with increases in temperature and lanthanide rare earth atomic number. At the same temperature, the coarsening rate K_{LSW} of parapath increases with the increase in atomic number, and the K_{LSW} of $Al_{11}RE_3$ phase in model1, 4, and 6 increases with the increase in temperature, which promotes the growth of particles.

Author Contributions: Conceptualization, L.L. and T.F.; Methodology, W.Y., L.L. and T.F.; Software, W.Y., L.L. and T.F.; Validation, W.Y., L.L., Z.L. and H.P.; Formal analysis, W.Y., L.L. and T.F.; Investigation, L.L. and T.F.; Resources, Y.L. and T.F.; Data curation, L.L., Y.W. (Yiru Wang) and T.F.; Writing—original draft, W.Y. and L.L.; Writing—review & editing, T.F.; Visualization, W.Y. and L.L.; Supervision, Y.W. (Yiru Wang) and T.F.; Project administration, W.Y., Y.L., L.C., T.F., Y.D., X.L. and D.C.; Funding acquisition, T.F., Y.W. (Yuanzhi Wu) and Y.D. All authors have read and agreed to the published version of the manuscript.

Funding: This research was funded by the Basic and Applied Basic Research Fund of Guangdong Province, grant number 2020B1515120093, the National Natural Science Foundation of China (Nos. 52371009, 52171115), the Natural Science Foundation of Hunan Province (No. 2022JJ30222), the Projects Supported by Scientific Research Fund of Hunan Provincial Education Department (Nos. 22A0621, 21A0564, HQ21016, HP21047), Innovation and entrepreneurship training program for college students (Nos. S202311528089, S202411528095, and S202311528159).

Institutional Review Board Statement: Not applicable.

Informed Consent Statement: Not applicable.

Data Availability Statement: Data is contained within the article.

Conflicts of Interest: The authors declare that they have no known competing financial interests or personal relationships that could have appeared to influence the work reported in this paper.

References

1. Marquis, E.; Seidman, D.N. Nanoscale structural evolution of Al_3Sc precipitates in Al (Sc) alloys. *Acta Mater.* **2001**, *49*, 1909–1919. [CrossRef]
2. Woodward, C.; Asta, M.; Kresse, G.; Hafner, J. Density of constitutional and thermal point defects in $L1_2$ Al_3Sc. *Phys. Rev. B* **2001**, *63*, 094103. [CrossRef]
3. Clouet, E.; Nastar, M.; Sigli, C. Nucleation of Al_3Zr and Al_3Sc in aluminum alloys: From kinetic Monte Carlo simulations to classical theory. *Phys. Rev. B* **2004**, *69*, 064109. [CrossRef]
4. Fu, L.; Ke, J.L.; Zhang, Q.; Tang, B.Y.; Peng, L.M.; Ding, W.J. Mechanical properties of $L1_2$ type Al_3X (X = Mg, Sc, Zr) from first-principles study. *Phys. Status Solidi* **2012**, *249*, 1510–1516. [CrossRef]
5. Choe, H.; Dunand, D.C. Synthesis, structure, and mechanical properties of Ni–Al and Ni–Cr–Al superalloy foams. *Acta Mater.* **2004**, *52*, 1283–1295. [CrossRef]
6. Nong, Z.-S.; Zhu, J.-C.; Yang, X.-W.; Cao, Y.; Lai, Z.-H.; Liu, Y. First-principles investigation of the elastic and electronic properties of the binary intermetallics in the Al–La alloy system. *Phys. B Condens. Matter* **2012**, *407*, 4706–4711. [CrossRef]
7. Yao, F.; Zhang, L.; Meng, J.; Liu, X.; Meng, J.; Zhang, H. Strategy to enhance intrinsic ductility and surface stability of Mg-Zn-R (R = La to Sm) alloys from a first-principles study. *Comput. Mater. Sci.* **2019**, *165*, 96–100. [CrossRef]
8. Azzeddine, H.; Hanna, A.; Dakhouche, A.; Rabahi, L.; Scharnagl, N.; Dopita, M.; Brisset, F.; Helbert, A.-L.; Baudin, T. Impact of rare-earth elements on the corrosion performance of binary magnesium alloys. *J. Alloys Compd.* **2020**, *829*, 154569. [CrossRef]
9. Tolley, A.; Radmilovic, V.; Dahmen, U. Segregation in Al_3 (Sc, Zr) precipitates in Al–Sc–Zr alloys. *Scr. Mater.* **2005**, *52*, 621–625. [CrossRef]
10. Li, J.; Oberdorfer, B.; Wurster, S.; Schumacher, P. Impurity effects on the nucleation and growth of primary Al_3 (Sc, Zr) phase in Al alloys. *J. Mater. Sci.* **2014**, *49*, 5961–5977. [CrossRef]
11. Hyde, K.; Norman, A.; Prangnell, P.B. The effect of Ti on grain refinement in Al-Sc alloys. In Proceedings of the Materials Science Forum, Cambridge, UK, 2–5 July 2002; pp. 39–44.
12. Nie, Z.R.; Jin, T.; Fu, J.; Xu, G.; Yang, J.; Zhou, J.X.; Zuo, T.Y. Research on rare earth in aluminum. In *Materials Science Forum*; Trans Tech Publications Ltd.: Zurich, Switzerland, 2002; p. 1731.
13. Meng, L.; Zheng, X. Overview of the effects of impurities and rare earth elements in Al-Li alloys. *Mater. Sci. Eng. A* **1997**, *237*, 109–118. [CrossRef]
14. Shi, Y.; Pan, Q.; Li, M.; Huang, X.; Li, B. Effect of Sc and Zr additions on corrosion behaviour of Al–Zn–Mg–Cu alloys. *J. Alloys Compd.* **2014**, *612*, 42–50. [CrossRef]
15. Murashkin, M.Y.; Sabirov, I.; Medvedev, A.; Enikeev, N.; Lefebvre, W.; Valiev, R.; Sauvage, X. Mechanical and electrical properties of an ultrafine grained Al–8.5 wt.% RE (RE = 5.4 wt.% Ce, 3.1 wt.% La) alloy processed by severe plastic deformation. *Mater. Des.* **2016**, *90*, 433–442. [CrossRef]
16. Pérez-Bustamante, R.; Reyna-Cruz, A.; Acosta-Peña, D.; Santillán-Rodríguez, C.; Matutes-Aquino, J.; Pérez-Bustamante, F.; Maldonado-Orozco, M.; Aguilar-Santillán, J.; Martínez-Sánchez, R. Effect of cerium/lanthanum addition on microstructure and mechanical properties of Al7075 alloy via mechanical alloying and sintering. *J. Rare Earths* **2016**, *34*, 420–427. [CrossRef]

17. Srivastava, V.C.; Surreddi, K.B.; Scudino, S.; Schowalter, M.; Uhlenwinkel, V.; Schulz, A.; Eckert, J.; Rosenauer, A.; Zoch, H.-W. Microstructural characteristics of spray formed and heat treated Al–(Y, La)–Ni–Co system. *J. Alloys Compd.* **2013**, *578*, 471–480. [CrossRef]
18. Amadeh, A.; Pahlevani, B.; Heshmati-Manesh, S. Effects of rare earth metal addition on surface morphology and corrosion resistance of hot-dipped zinc coatings. *Corros. Sci.* **2002**, *44*, 2321–2331. [CrossRef]
19. Rosalbino, F.; Angelini, E.; Macciò, D.; Saccone, A.; Delfino, S. Application of EIS to assess the effect of rare earths small addition on the corrosion behaviour of Zn–5% Al (Galfan) alloy in neutral aerated sodium chloride solution. *Electrochim. Acta* **2009**, *54*, 1204–1209. [CrossRef]
20. Zhang, X.; Wang, S. First-principles study of thermodynamic properties and solubility of aluminum-rare-earth intermetallics. *Comput. Mater. Sci.* **2014**, *90*, 56–60. [CrossRef]
21. Mao, Z.; Seidman, D.N.; Wolverton, C. First-principles phase stability, magnetic properties and solubility in aluminum–rare-earth (Al–RE) alloys and compounds. *Acta Mater.* **2011**, *59*, 3659–3666. [CrossRef]
22. Wu, Y.; Deng, B.; Li, X.; Li, Q.; Ye, T.; Xiang, S.; Zhao, M.-C.; Atrens, A. In-situ EBSD study on twinning activity caused by deep cryogenic treatment (DCT) for an as-cast AZ31 Mg alloy. *J. Mater. Res. Technol.* **2024**, *30*, 3840–3850. [CrossRef]
23. Vlach, M.; Čížek, J.; Smola, B.; Melikhova, O.; Vlček, M.; Kodetová, V.; Kudrnová, H.; Hruška, P. Heat treatment and age hardening of Al–Si–Mg–Mn commercial alloy with addition of Sc and Zr. *Mater. Charact.* **2017**, *129*, 1–8. [CrossRef]
24. Murty, B.; Kori, S.; Chakraborty, M. Grain refinement of aluminium and its alloys by heterogeneous nucleation and alloying. *Int. Mater. Rev.* **2002**, *47*, 3–29. [CrossRef]
25. Krug, M.E.; Werber, A.; Dunand, D.C.; Seidman, D.N. Core–shell nanoscale precipitates in Al–0.06 at.% Sc microalloyed with Tb, Ho, Tm or Lu. *Acta Mater.* **2010**, *58*, 134–145. [CrossRef]
26. Gao, Y.; Liu, G.; Sun, J. Recent progress in high-temperature resistant aluminum-based alloys: Microstructural design and precipitation strategy. *Acta Metall. Sin.* **2020**, *57*, 129–149.
27. Weakley-Bollin, S.; Donlon, W.; Donlon, W.; Wolverton, C.; Allison, J.; Jones, J.W. Modeling the age-hardening behavior of Al-Si-Cu alloys. *Metall. Mater. Trans. A* **2004**, *35*, 2407–2418. [CrossRef]
28. Polmear, I.; Couper, M.J. Design and development of an experimental wrought aluminum alloy for use at elevated temperatures. *Metall. Trans. A* **1988**, *19*, 1027–1035. [CrossRef]
29. Yang, J.; Heogh, W.; Ju, H.; Kang, S.; Jang, T.-S.; Jung, H.-D.; Jahazi, M.; Han, S.C.; Park, S.J.; Kim, H.S. Functionally graded structure of a nitride-strengthened Mg_2Si-based hybrid composite. *J. Magnes. Alloys* **2024**, *12*, 1239–1256. [CrossRef]
30. Suwanpreecha, C.; Toinin, J.P.; Michi, R.; Pandee, P.; Dunand, D.C.; Limmaneevichitr, C. Strengthening mechanisms in AlNiSc alloys containing Al_3Ni microfibers and Al_3Sc nanoprecipitates. *Acta Mater.* **2019**, *164*, 334–346. [CrossRef]
31. Pandey, P.; Makineni, S.K.; Gault, B.; Chattopadhyay, K. On the origin of a remarkable increase in the strength and stability of an Al rich Al-Ni eutectic alloy by Zr addition. *Acta Mater.* **2019**, *170*, 205–217. [CrossRef]
32. Suwanpreecha, C.; Pandee, P.; Patakham, U.; Limmaneevichitr, C. New generation of eutectic Al-Ni casting alloys for elevated temperature services. *Mater. Sci. Eng. A* **2018**, *709*, 46–54. [CrossRef]
33. Plotkowski, A.; Rios, O.; Sridharan, N.; Sims, Z.; Unocic, K.; Ott, R.; Dehoff, R.; Babu, S.J.A.M. Evaluation of an Al-Ce alloy for laser additive manufacturing. *Acta Mater.* **2017**, *126*, 507–519. [CrossRef]
34. Sims, Z.C.; Rios, O.R.; Weiss, D.; Turchi, P.E.; Perron, A.; Lee, J.R.; Li, T.T.; Hammons, J.A.; Bagge-Hansen, M.; Willey, T.M. High performance aluminum–cerium alloys for high-temperature applications. *Mater. Horiz.* **2017**, *4*, 1070–1078. [CrossRef]
35. Liu, Y.; Michi, R.A.; Dunand, D.C. Cast near-eutectic Al-12.5 wt.% Ce alloy with high coarsening and creep resistance. *Mater. Sci. Eng. A* **2019**, *767*, 138440. [CrossRef]
36. Sun, Y.; Hung, C.; Hebert, R.J.; Fennessy, C.; Tulyani, S.; Aindow, M. Eutectic microstructures in dilute Al-Ce and Al-Co alloys. *Mater. Charact.* **2019**, *154*, 269–276. [CrossRef]
37. Seidman, D.N.; Marquis, E.A.; Dunand, D.C. Precipitation strengthening at ambient and elevated temperatures of heat-treatable Al (Sc) alloys. *Acta Mater.* **2002**, *50*, 4021–4035. [CrossRef]
38. Booth-Morrison, C.; Mao, Z.; Diaz, M.; Dunand, D.; Wolverton, C.; Seidman, D. Role of silicon in accelerating the nucleation of Al_3 (Sc, Zr) precipitates in dilute Al–Sc–Zr alloys. *Acta Mater.* **2012**, *60*, 4740–4752. [CrossRef]
39. Vo, N.; Dunand, D.; Seidman, D. Improving aging and creep resistance in a dilute Al–Sc alloy by microalloying with Si, Zr and Er. *Acta Mater.* **2014**, *63*, 73–85. [CrossRef]
40. Vo, N.Q.; Dunand, D.C.; Seidman, D.N. Role of silicon in the precipitation kinetics of dilute Al-Sc-Er-Zr alloys. *Mater. Sci. Eng. A* **2016**, *677*, 485–495. [CrossRef]
41. Michi, R.A.; Toinin, J.P.; Farkoosh, A.R.; Seidman, D.N.; Dunand, D.C. Effects of Zn and Cr additions on precipitation and creep behavior of a dilute Al–Zr–Er–Si alloy. *Acta Mater.* **2019**, *181*, 249–261. [CrossRef]
42. Booth-Morrison, C.; Dunand, D.C.; Seidman, D.N. Coarsening resistance at 400 C of precipitation-strengthened Al–Zr–Sc–Er alloys. *Acta Mater.* **2011**, *59*, 7029–7042. [CrossRef]
43. Booth-Morrison, C.; Seidman, D.N.; Dunand, D.C. Effect of Er additions on ambient and high-temperature strength of precipitation-strengthened Al–Zr–Sc–Si alloys. *Acta Mater.* **2012**, *60*, 3643–3654. [CrossRef]
44. De Luca, A.; Seidman, D.N.; Dunand, D.C. Effects of Mo and Mn microadditions on strengthening and over-aging resistance of nanoprecipitation-strengthened Al-Zr-Sc-Er-Si alloys. *Acta Mater.* **2019**, *165*, 1–14. [CrossRef]

45. Vo, N.Q.; Seidman, D.N.; Dunand, D.C. Effect of Si micro-addition on creep resistance of a dilute Al-Sc-Zr-Er alloy. *Mater. Sci. Eng. A* **2018**, *734*, 27–33. [CrossRef]
46. De Luca, A.; Seidman, D.N.; Dunand, D.C. Mn and Mo additions to a dilute Al-Zr-Sc-Er-Si-based alloy to improve creep resistance through solid-solution-and precipitation-strengthening. *Acta Mater.* **2020**, *194*, 60–67. [CrossRef]
47. Nie, Z.R.; Wen, S.P.; Huang, H.; Li, B.L.; Zuo, T.Y. Research progress of er-containing aluminum alloy. *Chin. J. Nonferrous Metals* **2011**, *21*, 2361–2370.
48. Lv, S.; Li, Y.; Meng, F.; Duan, Q.; Yang, Q.; Liu, X.; Meng, J.J.C.M.S. Thermodynamic stability of Al11RE3 intermetallic compounds from first-principles calculations. *Comput. Mater. Sci.* **2017**, *131*, 28–34. [CrossRef]
49. Krug, M.E.; Dunand, D.C. Modeling the creep threshold stress due to climb of a dislocation in the stress field of a misfitting precipitate. *Acta Mater.* **2011**, *59*, 5125–5134. [CrossRef]
50. Buch, F.v.; Schumann, S.; Aghion, E.; Bronfin, B.; Mordike, B.; Bamberger, M.; Eliezer, D. Development of a Low-cost, Temperature- and Creep-resistant Magnesium Die-casting Alloy. *Magnes. Alloys Their Appl.* **2000**, 23–28. [CrossRef]
51. Rzychoń, T.; Kiełbus, A.; Lityńska-Dobrzyńska, L. Microstructure, microstructural stability and mechanical properties of sand-cast Mg–4Al–4RE alloy. *Mater. Charact.* **2013**, *83*, 21–34. [CrossRef]
52. Hu, T.; Ruan, Z.; Fan, T.; Wang, K.; He, K.; Wu, Y. First-principles investigation of the diffusion of TM and the nucleation and growth of $L1_2$ Al_3TM particles in Al alloys. *Crystals* **2023**, *13*, 1032. [CrossRef]
53. Hu, T.; Ruan, Z.; Fan, T.; Chen, D.; Wu, Y.; Tang, P. First-principles calculations to investigate stability, mechanical and thermodynamic properties of AlxTMy intermetallics in aluminum alloys. *Solid State Commun.* **2023**, *376*, 115361. [CrossRef]
54. Fan, T.; Lin, L.; Liang, H.; Ma, Y.; Tang, Y.; Hu, T.; Ruan, Z.; Chen, D.; Wu, Y. First-principles study of the structural, mechanical and thermodynamic properties of Al11RE3 in aluminum alloys. *Crystals* **2023**, *13*, 347. [CrossRef]
55. Fu, J.; Sun, J.; Cen, X.; Zhang, X.; Li, F.; Wu, Y. Growth behavior and orientation relationships in AISI 304 stainless steel during directional solidification. *Mater. Charact.* **2018**, *139*, 241–248. [CrossRef]
56. Hta, B.; Rui, Z.B.; Dong, Q.C.; Xin, L.B.; Qiu, F. Interfacial reaction behavior and evolution mechanism at a preoxidized SiCox/Al interface. *J. Mater. Res. Technol.* **2021**, *15*, 1100–1114.
57. Marder, M. Correlations and Ostwald ripening. *Phys. Rev. A* **1987**, *36*, 858. [CrossRef] [PubMed]
58. Czerwinski, F. Thermal Stability of Aluminum Alloys. *Materials* **2020**, *13*, 3441. [CrossRef] [PubMed]
59. Sun, S.; Li, X.; Wang, H.; Jiang, H.; Lei, W.; Jiang, Y.; Yi, D. First-principles investigations on the electronic properties and stabilities of low-index surfaces of $L1_2$-Al_3Sc intermetallic. *Appl. Surf. Sci.* **2014**, *288*, 609–618. [CrossRef]
60. Mantl, S.; Petry, W.; Schroeder, K.; Vogl, G. Diffusion of iron in aluminum studied by Mössbauer spectroscopy. *Phys. Rev. B* **1983**, *27*, 5313. [CrossRef]
61. Mao, Z.; Chen, W.; Seidman, D.N.; Wolverton, C. First-principles study of the nucleation and stability of ordered precipitates in ternary Al-Sc-Li alloys. *Acta Mater.* **2011**, *59*, 3012–3023. [CrossRef]
62. Hood, G.M. The diffusion of iron in aluminium. *Philos. Mag.* **1970**, *21*, 305–328. [CrossRef]
63. Finnis, M.W. REVIEW ARTICLE: The theory of metal-ceramic interfaces. *J. Phys. Condens. Matter* **1996**, *8*, 5811–5836. [CrossRef]
64. Wang, C.; Wang, C.Y. Ni/Ni_3Al interface: A density functional theory study. *Appl. Surf. Sci.* **2009**, *255*, 3669–3675. [CrossRef]
65. Zhou, W.F.; Ren, X.D.; Ren, Y.P.; Yuan, S.Q.; Ren, N.F.; Yang, X.Q.; Adu-Gyamfi, S. Initial dislocation density effect on strain hardening in FCC aluminium alloy under laser shock peening. *Philos. Mag.* **2017**, *97*, 1285073. [CrossRef]
66. Zhao, S.J.; Stocks, G.M.; Zhang, Y.W. Stacking fault energies of face-centered cubic concentrated solid solution alloys. *Acta Mater.* **2017**, *134*, 334–345. [CrossRef]
67. Dong, T.H.; Zhang, X.D.; Yang, L.M.; Wang, F. Effect of structural vacancies on lattice vibration, mechanical, electronic, and thermodynamic properties of Cr_5BSi_3. *Chin. Phys. B* **2022**, *31*, 026101. [CrossRef]
68. Liu, Y.Z.; Zhang, X.D.; Bi, H.J.; Liu, X.Q.; Wang, F. First-principles prediction of structure, mechanical and thermodynamic properties of $Bi_xGe_yO_z$ ternary bismuth crystals. *Vacuum* **2022**, *195*, 110696. [CrossRef]
69. Zhang, X.; Zhao, H.L.; Gao, S.; Zeng, Q.F. First-principles study of electronic structure and optical properties of Er: Lu_2O_3. *J. Rare Earths* **2021**, *39*, 453–459. [CrossRef]
70. Bao, L.H.; Ning, J.; Liu, Z.Z. Mechanism for transmittance light tunable property of nanocrystalline Eu-doped SmB_6: Experimental and first-principles study. *J. Rare Earths* **2021**, *39*, 1100–1107. [CrossRef]
71. Liu, X.M.; Wang, Q.; Zhao, C.; Li, H.P.; Wang, M.L.; Chen, D.; Wang, H.W. Formation of ordered precipitates in Al-Sc-Er-(Si/Zr) alloy from first-principles study. *J. Rare Earths* **2021**, *39*, 609–620. [CrossRef]
72. Hafner, J. Ab-initio simulations of materials using vasp: Density-functional theory and beyond. *J. Comp. Chem.* **2008**, *29*, 2044–2078. [CrossRef]
73. Blöchl, P.E. Projector augmented-wave method. *Phys. Rev. B* **1994**, *50*, 17953. [CrossRef] [PubMed]
74. Kresse, G.; Joubert, D. From ultrasoft pseudopotentials to the projector augmented-wave method. *Phys. Rev. B* **1999**, *59*, 1758. [CrossRef]
75. Perdew, J.P.; Burke, K.; Wang, Y. Generalized gradient approximation for the exchange-correlation hole of a many-electron system. *Phys. Rev. B* **1996**, *54*, 16533. [CrossRef] [PubMed]
76. Monkhorst, H.J.; Pack, J.D. Special points for Brillouin-zone integrations. *Phys. Rev. B* **1976**, *13*, 5188. [CrossRef]
77. Akkermans, R.L.; Spenley, N.A.; Robertson, S.H. Monte Carlo methods in materials studio. *Mol. Simul.* **2013**, *39*, 1153–1164. [CrossRef]

78. Hutchinson, J. Singular behaviour at the end of a tensile crack in a hardening material. *J. Mech. Phys. Solids* **1968**, *16*, 13–31. [CrossRef]
79. Rice, J.R.; Rosengren, G. Plane strain deformation near a crack tip in a power-law hardening material. *J. Mech. Phys. Solids* **1968**, *16*, 1–12. [CrossRef]
80. Li, J.; Zhang, M.; Zhou, Y.; Chen, G. First-principles study of Al/A13Ti heterogeneous nucleation interface. *Appl. Surf. Sci.* **2014**, *307*, 593–600. [CrossRef]
81. Siegel, D.J.; Hector, L.G., Jr.; Adams, J.B. Adhesion, stability, and bonding at metal/metal-carbide interfaces: Al/WC. *Surf. Sci.* **2002**, *498*, 321–336. [CrossRef]
82. Rapcewicz, K.; Chen, B.; Yakobson, B.; Bernholc, J. Consistent methodology for calculating surface and interface energies. *Phys. Rev. B* **1998**, *57*, 7281. [CrossRef]
83. Han, Y.; Dai, Y.; Shu, D.; Wang, J.; Sun, B. First-principles study of TiB_2 (0001) surfaces. *J. Phys. Condens. Matter* **2006**, *18*, 4197. [CrossRef] [PubMed]
84. Li, S.-S.; Li, L.; Han, J.; Wang, C.-T.; Xiao, Y.-Q.; Jian, X.-D.; Qian, P.; Su, Y.-J. First-Principles study on the nucleation of precipitates in ternary Al alloys doped with Sc, Li, Zr, and Ti elements. *Appl. Surf. Sci.* **2020**, *526*, 146455. [CrossRef]
85. Kaya, M.; Ceyhan, A.A.; Şahin, Ö. Effects of different temperatures and additives on the metastable zone width precipitation kinetics of $NaBO_2$. *Russ. J. Phys. Chem. A* **2014**, *88*, 402–408. [CrossRef]
86. Ozoliņš, V.; Wolverton, C.; Zunger, A. Cu-Au, Ag-Au, Cu-Ag, and Ni-Au intermetallics: First-principles study of temperature-composition phase diagrams and structures. *Phys. Rev. B* **1998**, *57*, 6427. [CrossRef]
87. Zhang, C.; Peng, P.; Lv, H.; Gao, H.; Wang, Y.; Wang, J.; Sun, B. Orientation relationships and interface structure between $Al_{11}Ce_3$ and Al in Al–Ce eutectic. *J. Mater. Res. Technol.* **2022**, *18*, 693–704. [CrossRef]
88. Togo, A.; Tanaka, I. First principles phonon calculations in materials science. *Scr. Mater.* **2015**, *108*, 1–5. [CrossRef]
89. Zhou, Z.; Wu, B.; Dou, S.; Zhao, C.; Xiong, Y.; Wu, Y.; Yang, S.; Wei, Z. Thermodynamic Properties of Elements and Compounds in Al-Sc Binary System from Ab Initio Calculations Based on Density Functional Theory. *Metall. Mater. Trans. A* **2014**, *45*, 1720–1735. [CrossRef]
90. Lifshitz, I.M.; Slyozov, V.V. The kinetics of precipitation from supersaturated solid solutions. *J. Phys. Chem. Solids* **1961**, *19*, 35–50. [CrossRef]
91. Wagner, C. Zeitschrift für Elektrochemie. *Berichte Bunsenges. Phys. Chem.* **1961**, *65*, 7–8.

Disclaimer/Publisher's Note: The statements, opinions and data contained in all publications are solely those of the individual author(s) and contributor(s) and not of MDPI and/or the editor(s). MDPI and/or the editor(s) disclaim responsibility for any injury to people or property resulting from any ideas, methods, instructions or products referred to in the content.